

# Electronic Supplementary Information

## **Nickel single atoms anchored on bipyridine covalent organic framework: Boosting active sites for photodegradation of acetaminophen**

Guijiao Wen<sup>a</sup>, Qianqian Peng<sup>a</sup>, Chen Yuan<sup>a</sup>, Juan He<sup>a\*</sup>, Xiandeng Hou<sup>a b\*</sup>

<sup>a</sup>Analytical & Testing Center, Sichuan University, Chengdu 610064, Sichuan, China

<sup>b</sup>College of Chemistry, Sichuan University, Chengdu 610064, Sichuan, China

\*Corresponding author: [houxd@scu.edu.cn](mailto:houxid@scu.edu.cn); [hejuan1117@scu.edu.cn](mailto:hejuan1117@scu.edu.cn)

## Contents

1. Materials .....	3
2. Characterization .....	3
3. DFT calculations.....	4
4. Details of LC-MS analysis.....	5
5. Figures .....	7
6. Tables.....	19
6.1 Structural EXAFS data fitting results of Samples .....	19
6.2 Photoluminescent lifetime determination .....	21
6.3 Comparison of the photocatalytic performance.....	22
6.4 Actual amount of Ni anchored on the TpBpy.....	23
6.5 Intermediates products.....	24
7. Reference .....	25

## 1. Materials

All chemicals were obtained from commercial sources and used without further purification. 2,2'-Bipyridine-5,5'-diamine (Bpy, >99 %) was purchased from Jilin Chinese Academy of Sciences-Yanshen Technology Co, Ltd (Jilin, China). N, N-dimethylacetamide (DMAc, 99.8 %, Extra Day, with molecular sieves, water  $\leq 50$  ppm) was purchased from Energy Chemical (Anhui, China). O-dichlorobenzene (o-DCB, 99 %), 1,3,5-triformylphloroglucinol (Tp, > 97 %), acetic acid (AcOH,  $\geq 99.8$  %), Ni (ClO<sub>4</sub>)<sub>2</sub>·6H<sub>2</sub>O (99.9 % trace metals basis), sulfamethoxazole (SMX), sulfisoxazole (SIZ), sulfathiazole (STZ) and acetaminophen (99% pure Bio extra) were obtained from Aladdin Reagent Co (Shanghai, China). 2, 2, 6, 6-Tetramethylpiperidine (TEMP), sodium sulfate anhydrous (Na<sub>2</sub>SO<sub>4</sub>), ethylenediaminetetraacetic acid disodium salt dihydrate (EDTA-2Na), isopropyl alcohol (IPA), and benzoquinone (BQ) were purchased from Chron Chemicals (Chengdu, China). 5, 5-Dimethyl-1-pyrroline N-oxide (DMPO) was purchased from Dojindo Co. (Shanghai, China).

## 2. Characterization

The Ni content of Ni-TpBpy was measured using an inductively coupled plasma-optical emission spectrometer (ICP-OES, 5100 SVDV Series, Agilent, USA). The crystalline structure was studied with a powder X-ray diffractometer (Panalytical, Netherlands) employing Cu K $\alpha$  lines with the scanned range from 1° to 60°. The infrared spectra of the samples were recorded using a Nicolet 6700 Fourier transform infrared spectrometer (FT-IR, Thermoelectronics, USA) with scanned range from 4000 to 400 cm<sup>-1</sup>. The morphology and elemental distribution of the samples were obtained with the scanning electron microscopy (SEM, JEOL, Japan) on a JSM-7500F apparatus equipped with an energy dispersive spectrometer (EDS). The microstructure was investigated using high-resolution transmission electron microscopy (HRTEM, Tecnai G2 F20, FEI, USA). N<sub>2</sub> adsorption-desorption isotherms at 77 K were executed on the ASAP 2020 instrument (Micromeritics, USA).

The surface chemical state of the samples was analyzed using AXIS Ultra DLD clutches X-ray photoelectron spectrometer (XPS, Kratos, UK). The photoluminescence (PL) spectra were detected by using the F-7000 (Hitachi, Japan) with an excitation wavelength of 420 nm. Time-resolved fluorescence measurements were performed on an (Horiba Jobin Yvon) instrument at an excitation wavelength of 406 nm. The total organic carbon (TOC) was measured with a TOC analyzer (Vario TOC select, Germany Elementar). The UV-vis diffuse reflectance spectra (UV-vis DRS) of the samples were measured using the UV 3600 spectrophotometer (Shimadzu, Japan). The scanned range was from 200 to 1500 nm and BaSO<sub>4</sub> was used as the reference for baseline correction. The electron spin resonance spectra were obtained in EMXplus X-band EPR (Bruker, Germany).

### 3. DFT calculations

The nonlocal generalized gradient approximation (GGA) function by employing the Perdew-Burke-Ernzerhof (PBE) correlation function<sup>1</sup> was used to calculate the exchange and correlation energy<sup>2</sup>. The convergence criteria for geometry optimization were set to the tolerance for the energy, maximum force, maximum displacement and SCF on all atoms of  $2.0 \times 10^{-5}$  Ha, 0.004 Ha/Å, 0.005 Å and  $1.0 \times 10^{-6}$  Ha, respectively. A cut-off energy of 400 eV was used for the plane-wave basis set.

Spin-polarized calculations were employed with the double numerical polarization basis set. To accommodate the van der Waals interactions, the semi-empirical Tkatchenko-Scheffler (TS) scheme was included for dispersion correction. DFT semi-core pseudopotential was applied for the core-electron treatment. Brillouin zone was sampled by Monkhorst-Pack grid as  $\Gamma$ -point for all systems. The SCF convergence for each electronic energy was set as  $1.0 \times 10^{-6}$  Ha, and the geometry optimization convergence criteria were set up as follows:  $1.0 \times 10^{-5}$  Ha for energy, 0.002 Ha Å<sup>-1</sup> for force, and 0.005 Å for displacement, respectively. Li-ion migration pathways were examined by linear and quadratic synchronous transit (LST/QST) methods in combination with the conjugated gradient (CG) refinement.

The electronic structures of TpBpy and Ni-TpBpy as well as O<sub>2</sub> adsorbed in the

Ni-TpBpy at different charge states were studied by density functional theory (DFT), where all structures were optimized by the PBE0 functional and def2-SVP basis set by Gaussian 16 C.02 package. The long-range van der Waals (vdW) interactions were handled by Grimme's DFT-D3 scheme. Harmonic vibrational frequency was performed at the same level to guarantee that there is no imaginary frequency, i.e. they locate on the minima of the potential energy surface. The adsorption energy,  $E_{\text{ads}}$ , was evaluated as follows:

$$E_{\text{ads}}=E(\text{Ni-TpBpy}-\text{O}_2)-E(\text{Ni-TpBpy})-E(\text{O}_2) \quad (1)$$

where the terms at right hand are the single point energies of the dimer that is composed of Ni-TpBpy and O<sub>2</sub>, Ni-TpBpy and O<sub>2</sub>, respectively. The charge density difference was written as:

$$\Delta\rho=\rho(\text{Ni-TpBpy}-\text{O}_2)-\rho(\text{Ni-TpBpy})-\rho(\text{O}_2) \quad (2)$$

where the  $\rho(\text{Ni-TpBpy}-\text{O}_2)$ ,  $\rho(\text{Ni-TpBpy})$ , and  $\rho(\text{O}_2)$  are electron density of Ni-TpBpy -O<sub>2</sub>, Ni-TpBpy, and O<sub>2</sub>, respectively. The HOMO (Highest occupied molecular orbital), LUMO (Lowest unoccupied molecular orbital), and Bader atomic charges were calculated by Multiwfn 3.8 (dev), whose input files were extracted from Gaussian formatting checkpoint files at M06-2X/def2-TZVP, and the two formers were plotted by VMD 1.9.3. The electron-hole analysis was also calculated by Multiwfn 3.8 at PBE0-TD-D3(BJ)/def2-SVP level of theory.

Based on the DFT calculation, Fukui index was employed to predict the reactive sites for radical ( $f^0$ ) attack<sup>3</sup>.

#### 4. Details of LC-MS analysis

Ultra-high-performance liquid chromatography (UHPLC, Dionex UltiMate 3000 127 Series) coupled with an Orbitrap mass spectrometer (MS, Thermo Scientific, USA) was used for the determination of intermediate products generated during the photocatalytic process. Each injection volume of the sample was 10  $\mu\text{L}$ , and the chromatographic separation was using thermo C18 column (2.1 mm  $\times$  100 mm, particle size 1.9  $\mu\text{m}$ ) with a flow rate of 0.26 mL/min. The mobile phase was composed of solvent A (0.1% formic acid solution) and solution B (Nitrile solution)

for acetaminophen. Linear gradient elution steps were initially started with A 10% for 5 min, then increased linearly to 90% within 10 min and kept for 2 min, followed by decreasing linearly to 10% within 0.1 min and kept for 3 min. The mass spectrometer was operated in the positive ion mode ( $[M-H]^+$  ion). The determination of intermediate products was achieved under a selective ion recording (SIR) mode. The scan range of  $m/z$  100–500 was used for acetaminophen.

## 5. Figures

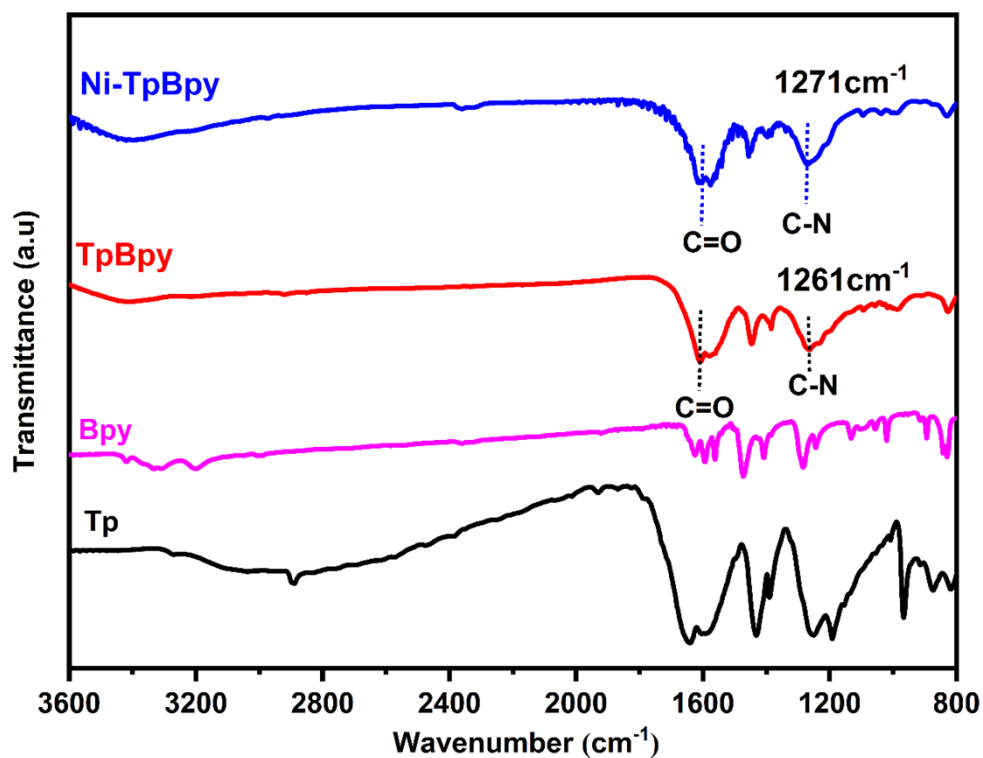


Fig. S1 FT-IR spectra of Tp, Bpy, TpBpy and Ni-TpBpy.

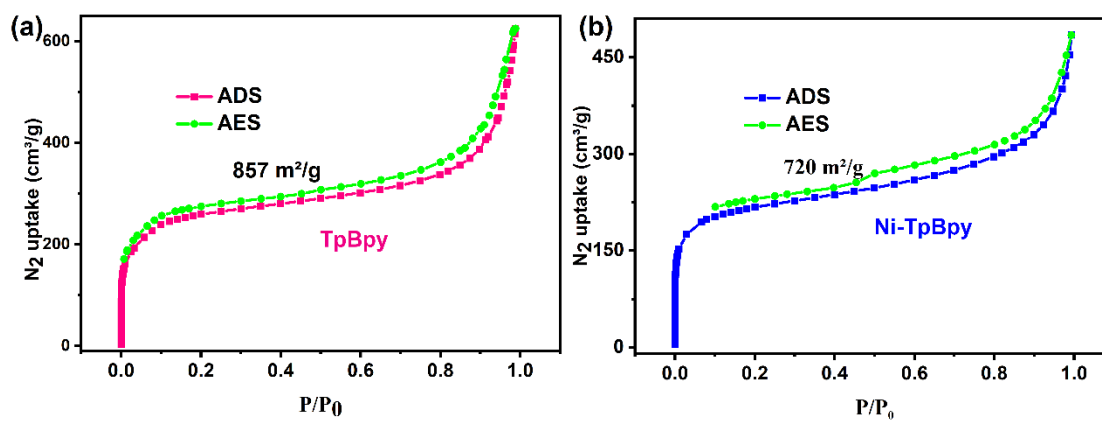
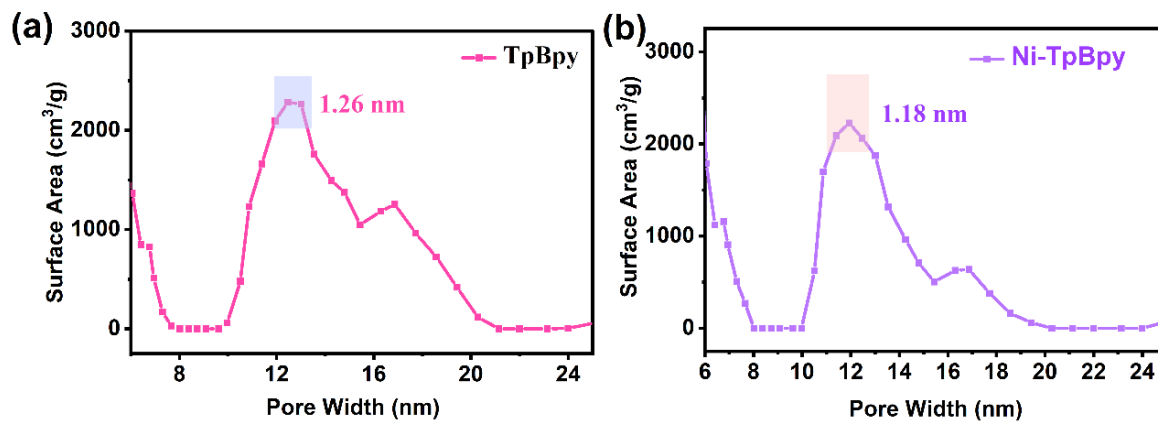
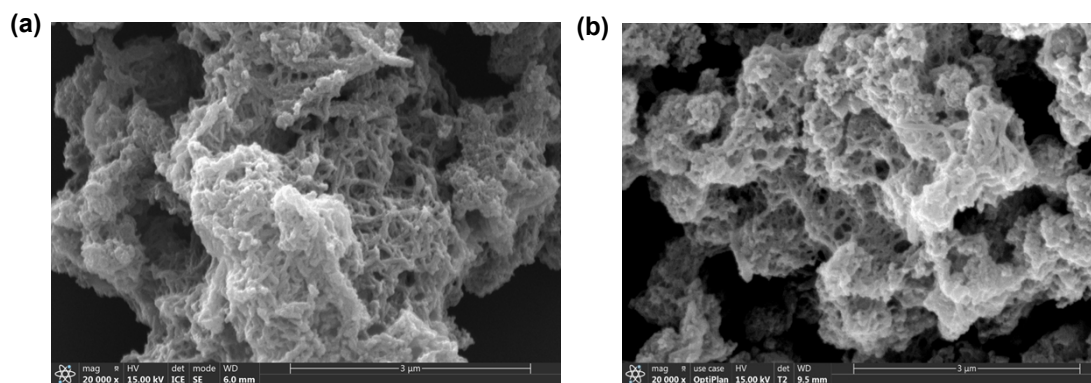


Fig. S2  $\text{N}_2$  adsorption/desorption isotherms of TpBpy (a) and Ni-TpBpy (b).



**Fig. S3** Pore size distributions of TpBpy (a) and Ni-TpBpy (b).



**Fig. S4** SEM image of TpBpy (a) and Ni-TpBpy (b).



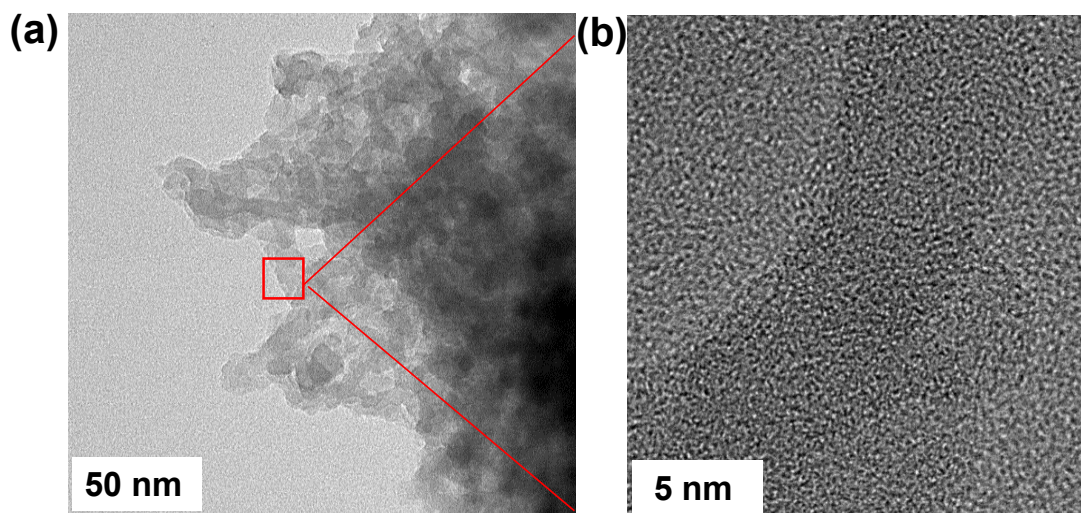


**Fig. S5** HRTEM image of Ni-TpBpy.

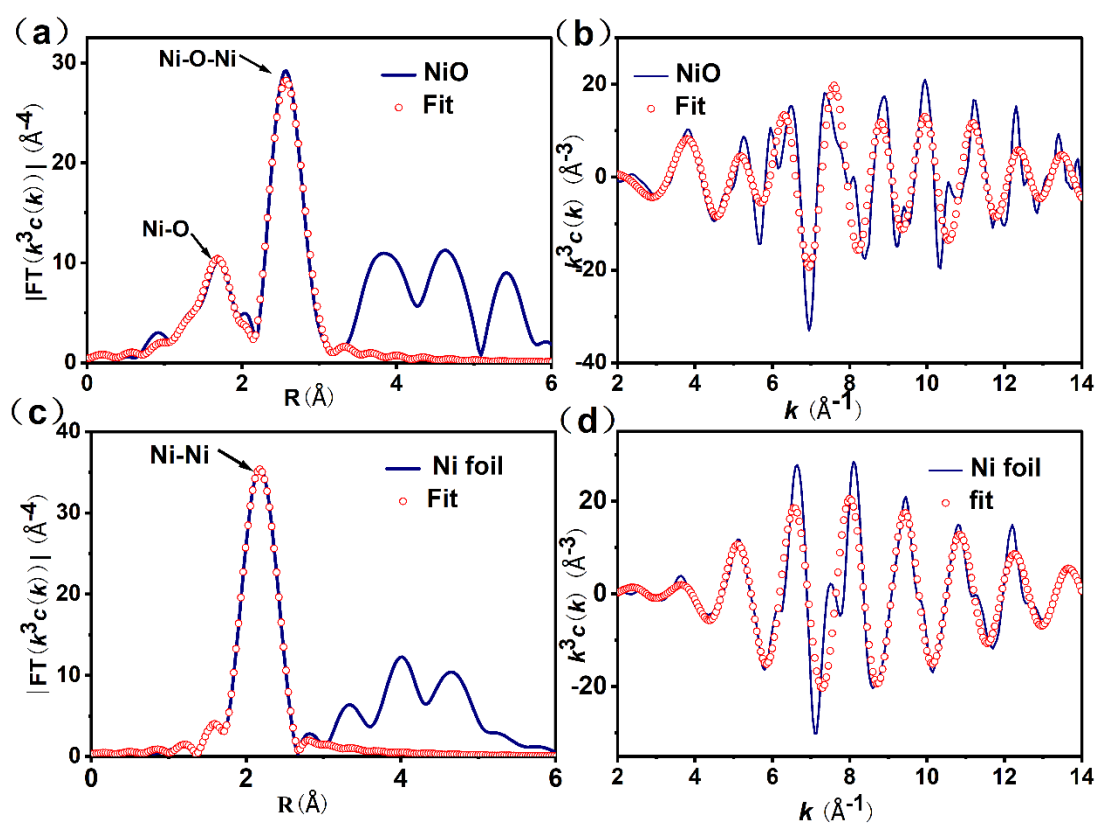


**Fig. S6** Fourier-transformed magnitudes of Ni L-edge EXAFS spectra in R space and k space for NiO (a, b) and Ni foil (c, d).

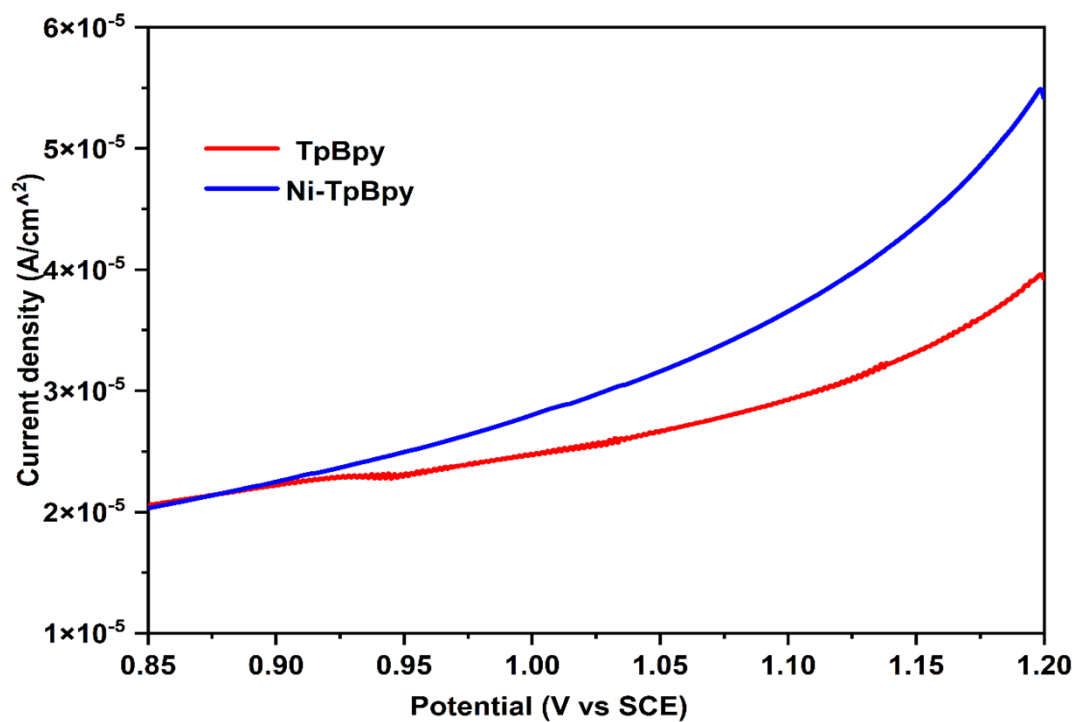


Fig. S7 Linear sweep voltammetry (LSV) curves of TpBpy and Ni-TpBpy.

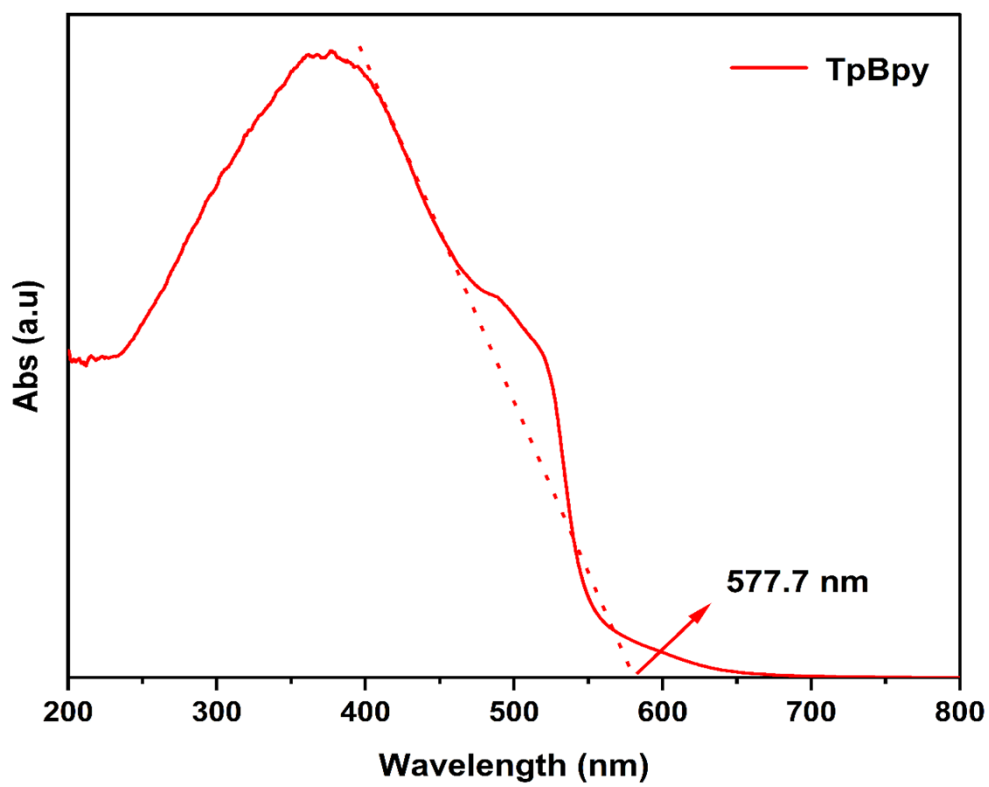


Fig. S8 UV-vis diffuse reflectance spectra of TpBpy.

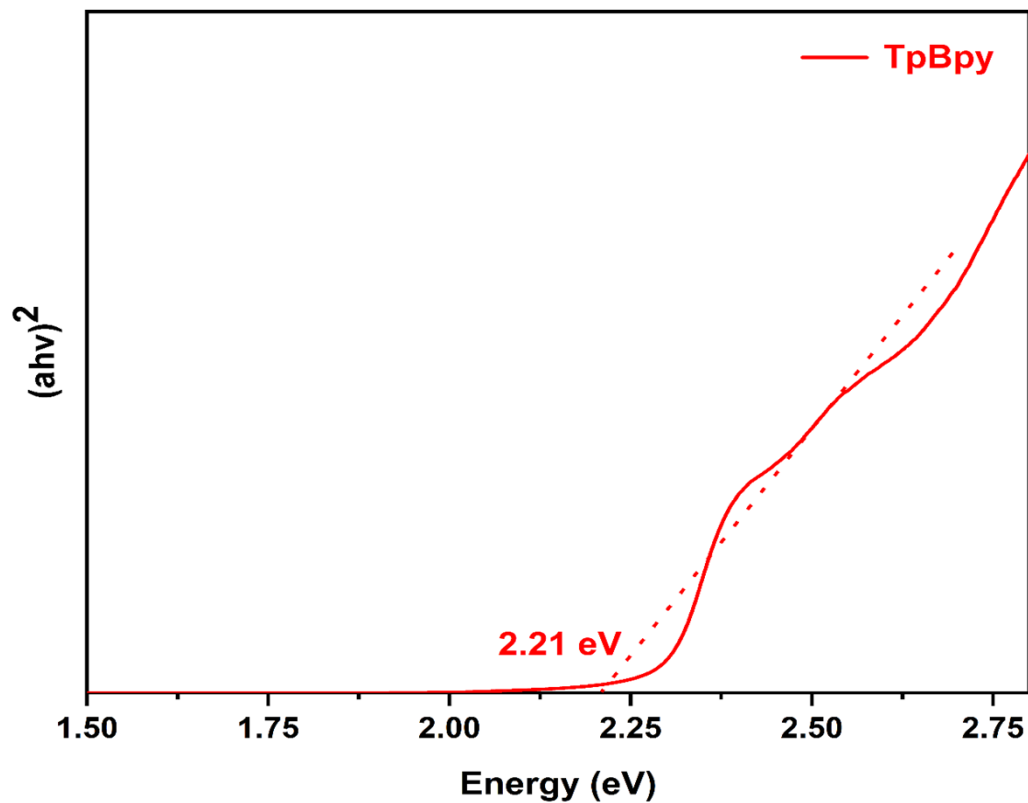


Fig. S9 Band gap energy of TpBpy.

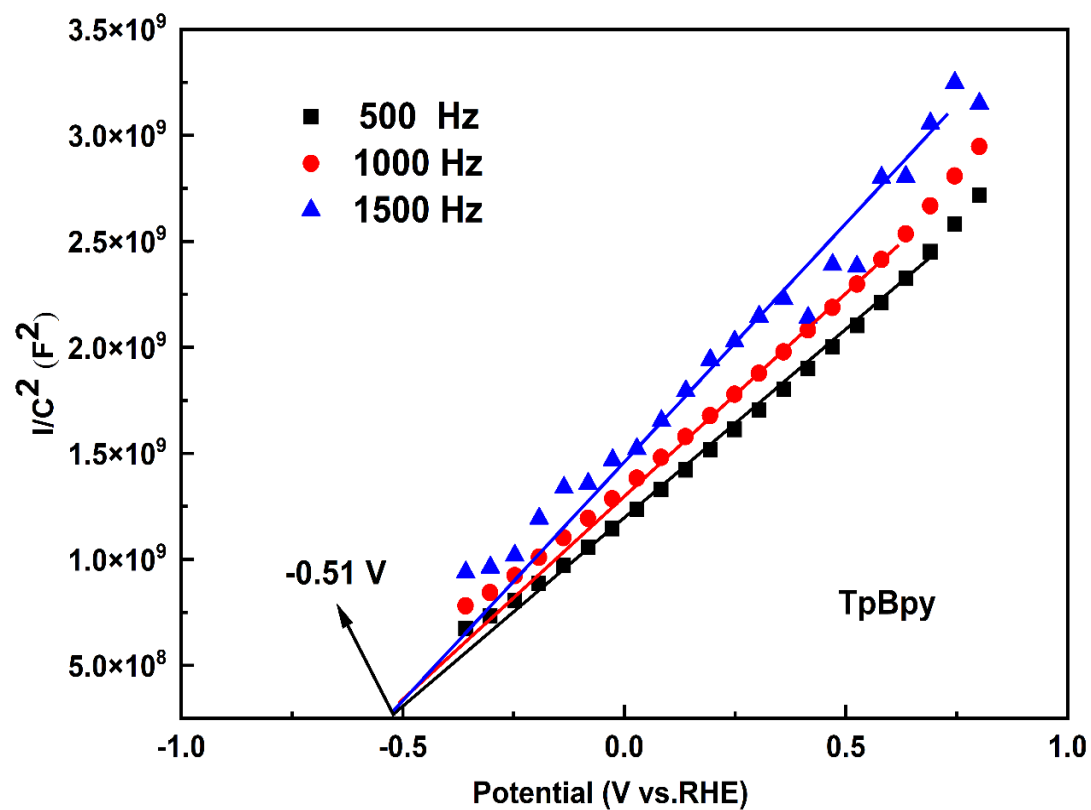
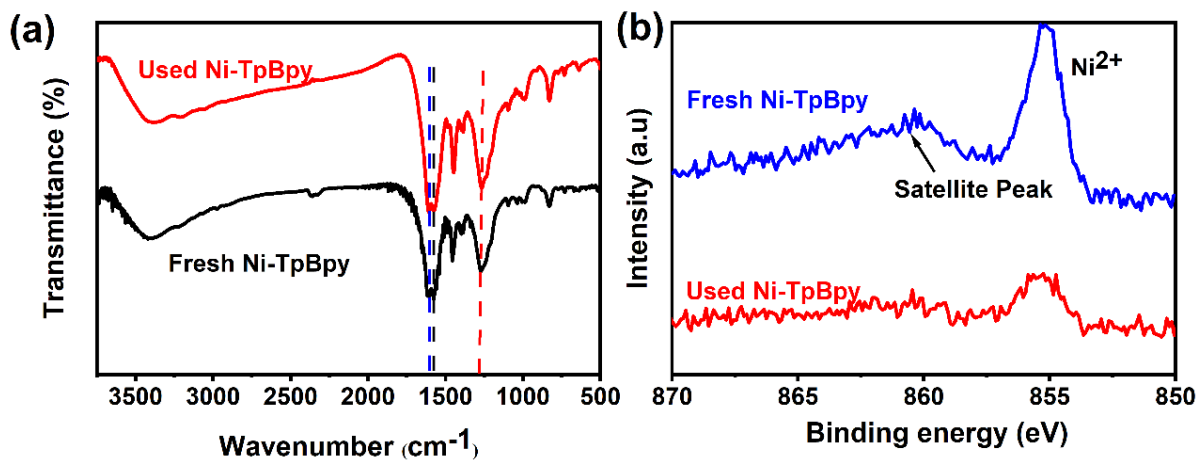
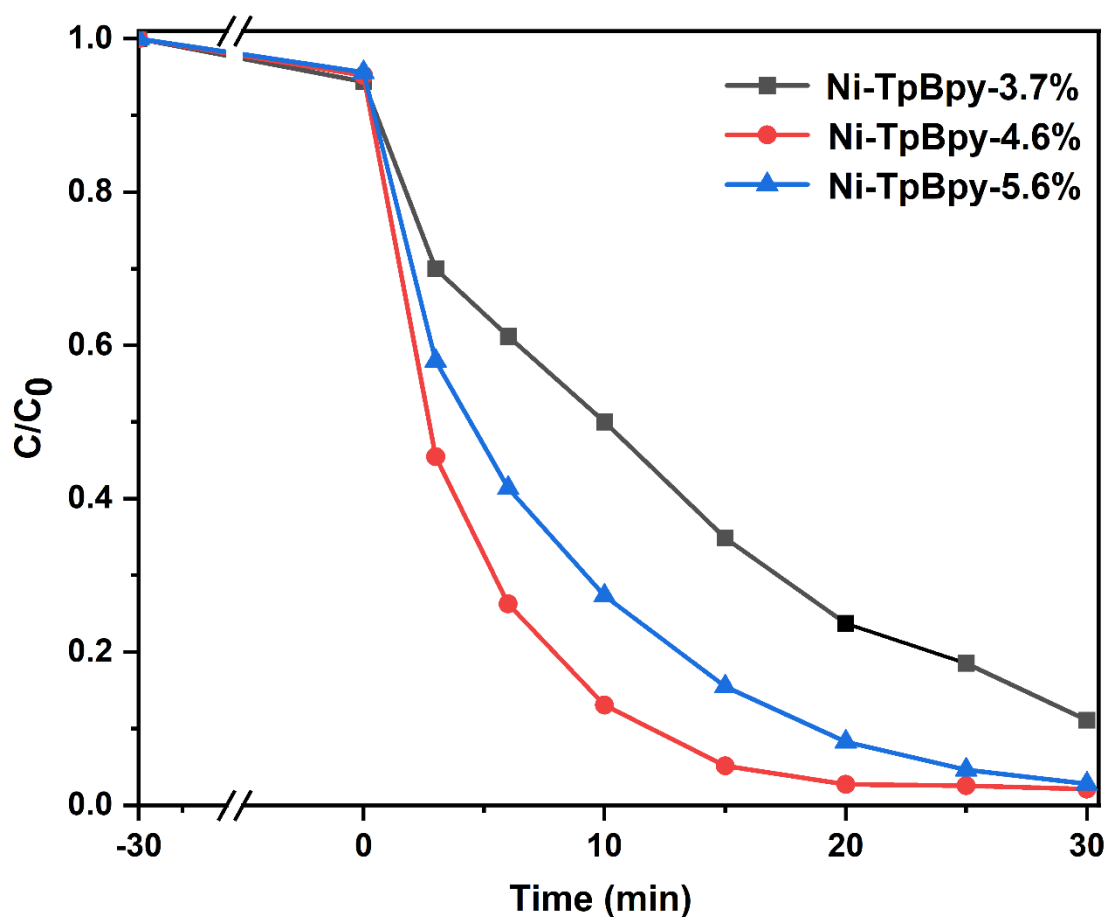


Fig. S10 Mott-Schottky curves of TpBpy.



**Fig. S11** FT-IR spectra (a) and Ni 2p XPS spectra (b) of Ni-TpBpy before and after 5 cycles experiments.



**Fig. S12** Effect of single atom loading on the photocatalytic performance of Ni-TpBpy.

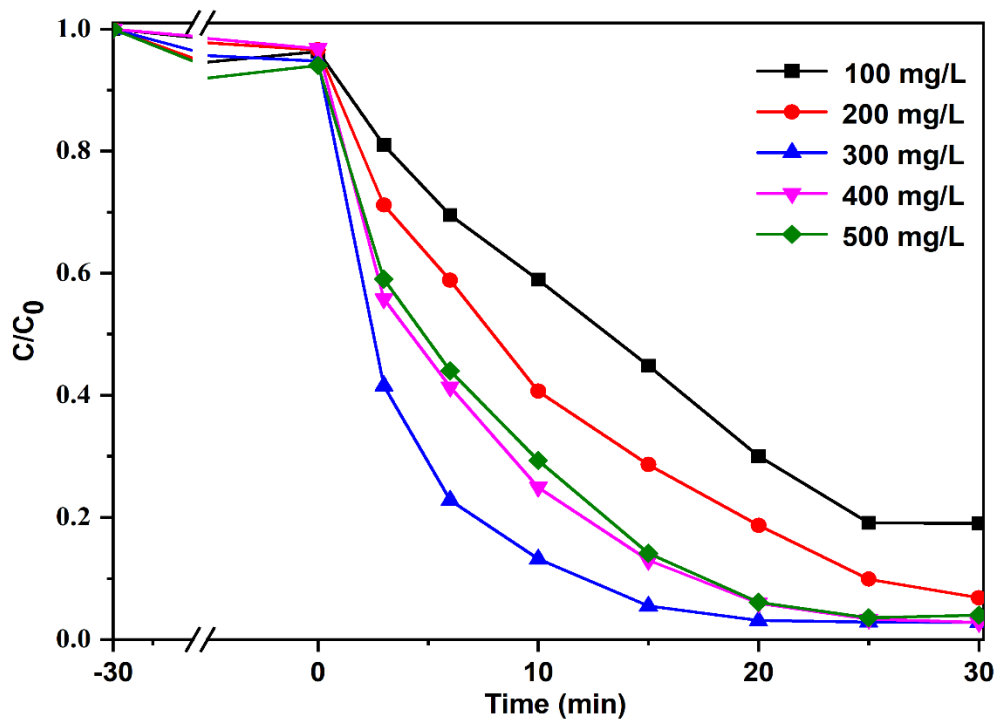


**Fig. S13** Effect of Ni-TpBpy concentration on the photocatalytic performance of Ni-TpBpy.

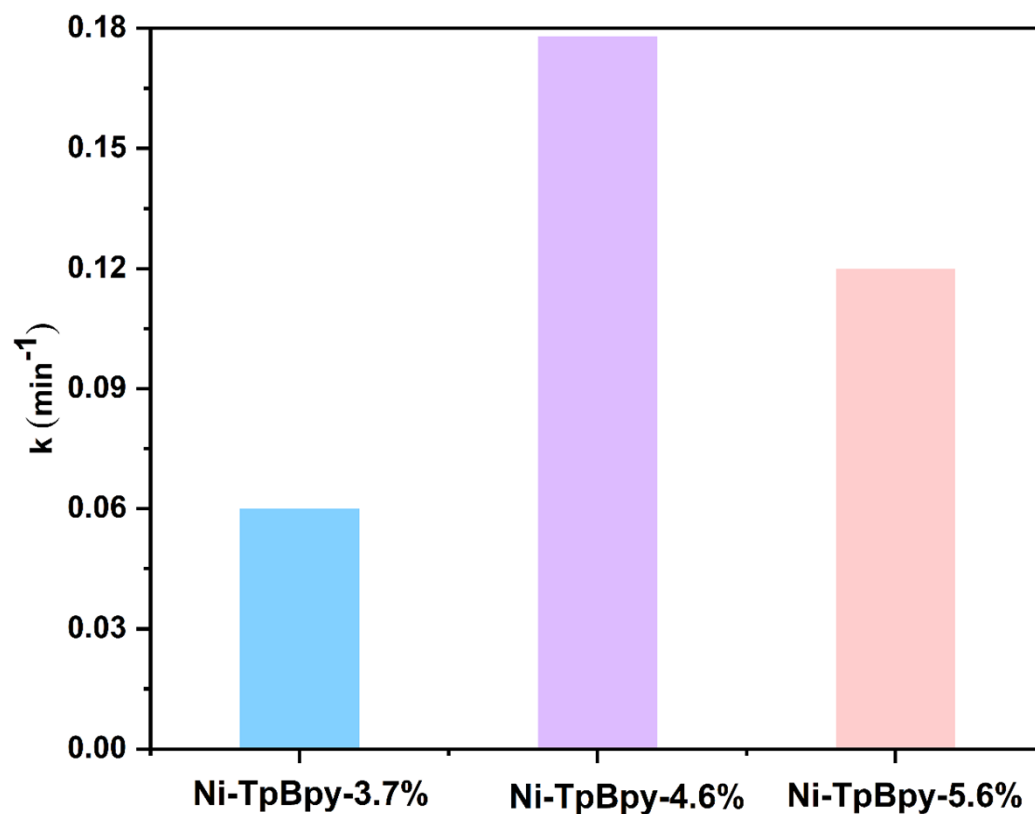


**Fig. S14** Effect of single-atom loading on the kinetic constant.

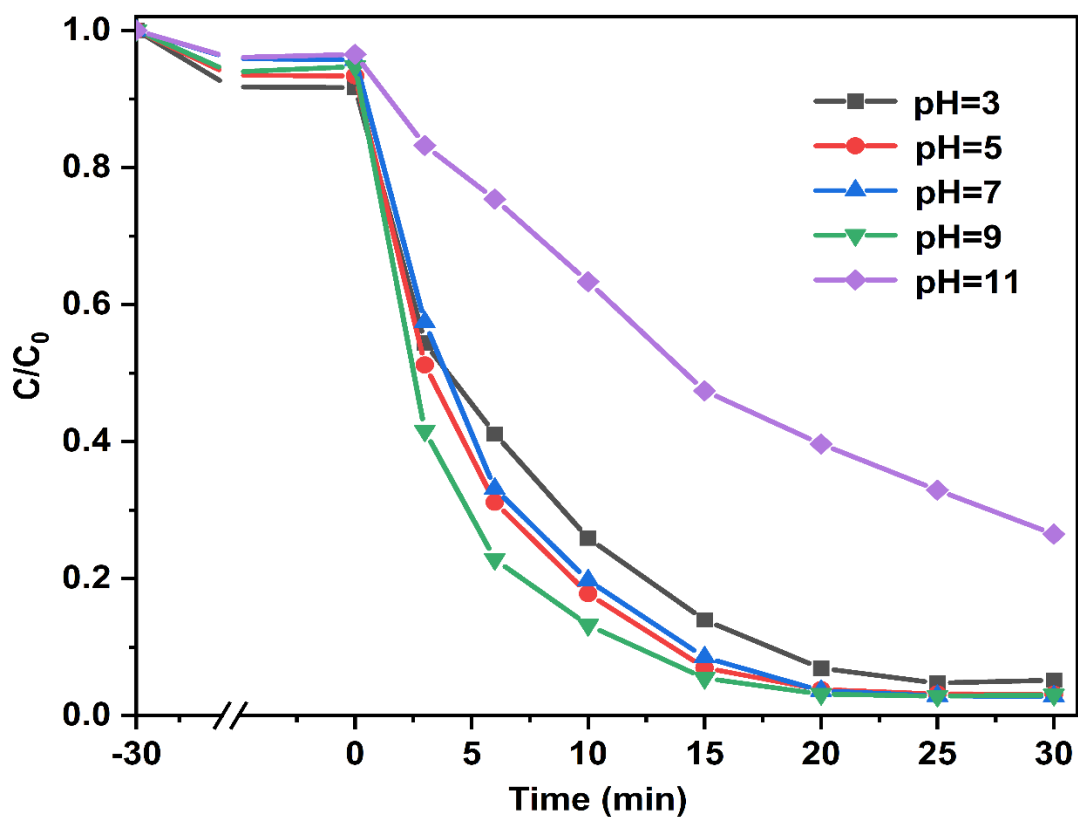


Fig. S15 Effect of pH on the photocatalytic performance of Ni-TpBpy.

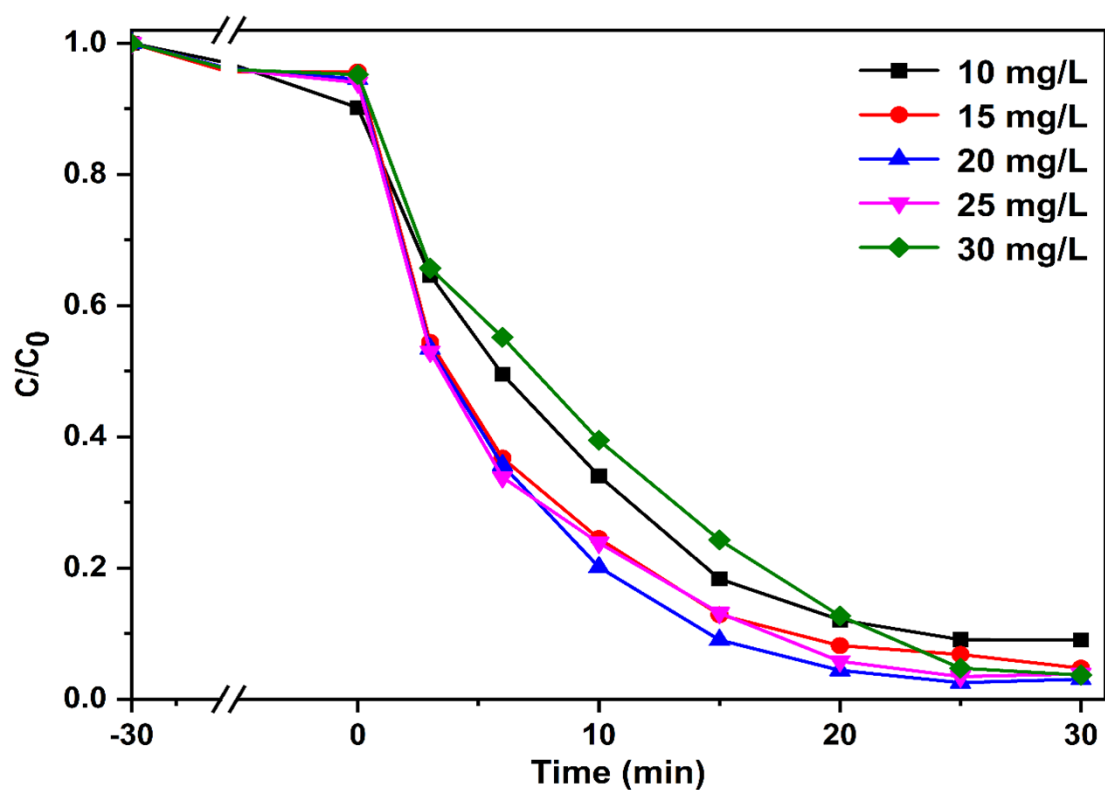


Fig. S16 Effect of ACT concentration on the photocatalytic performance of Ni-TpBpy.

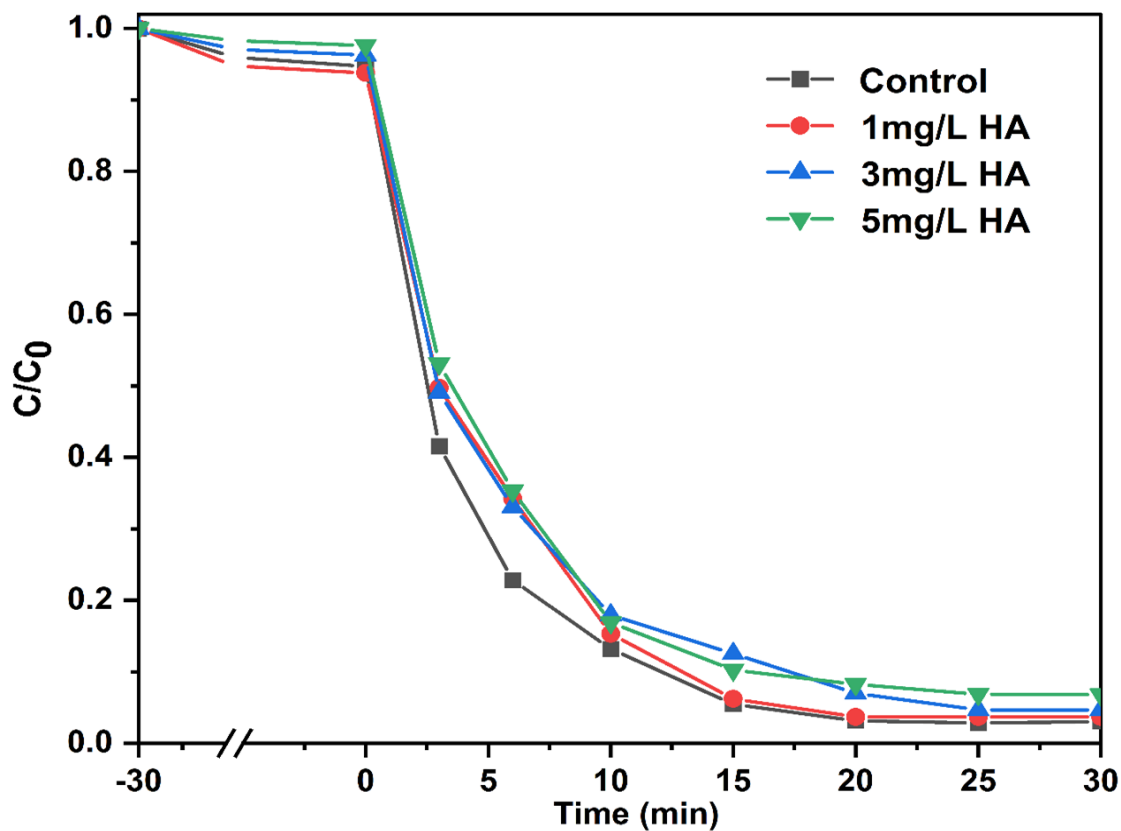


Fig. S17 Effect of HA concentration.

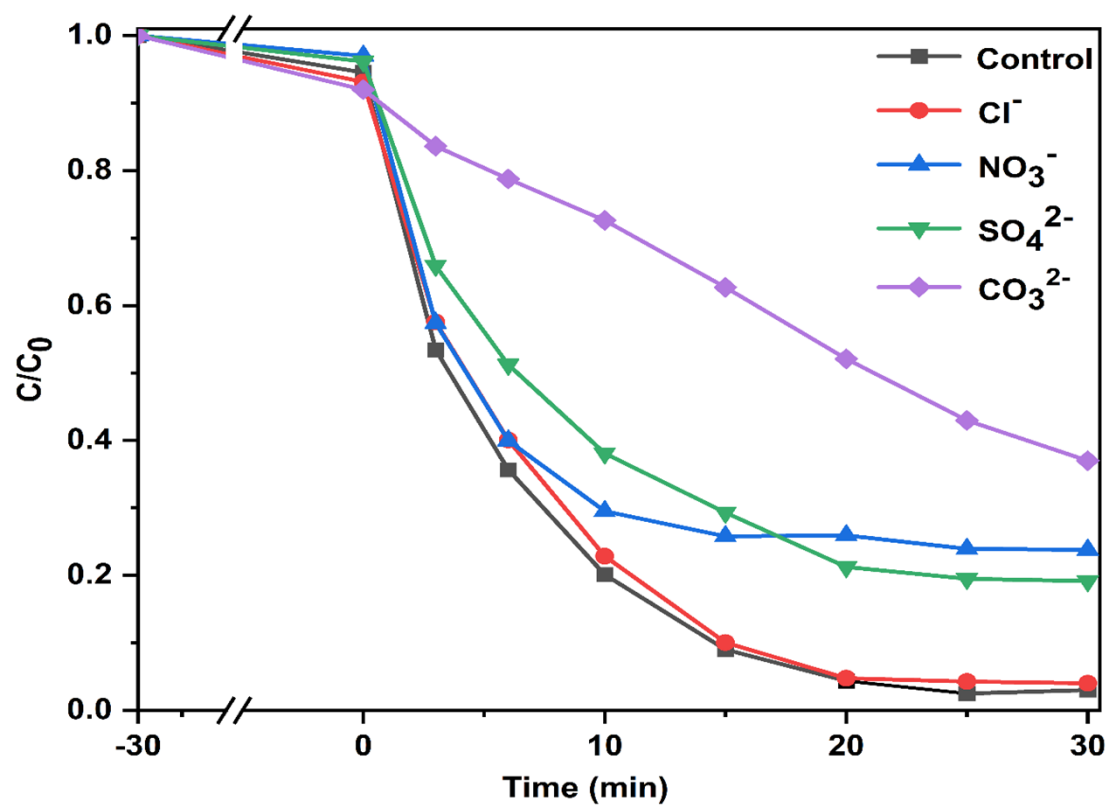
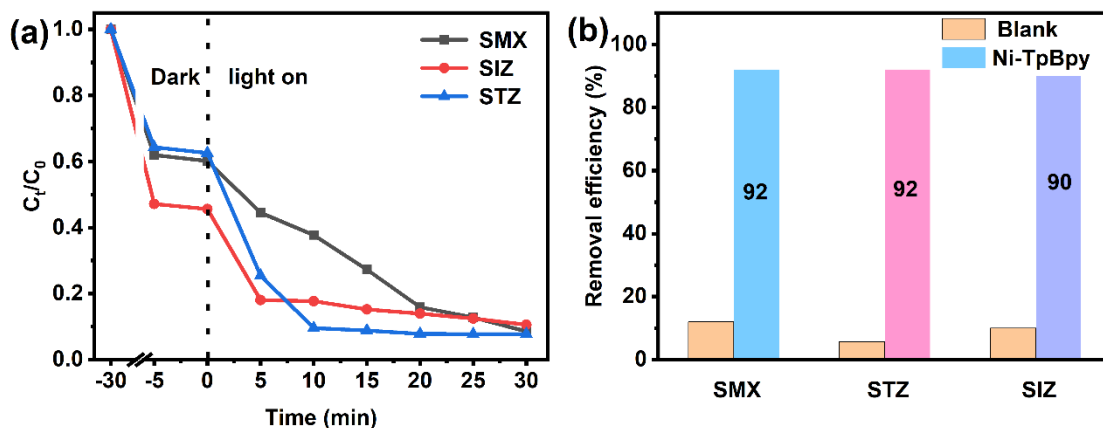
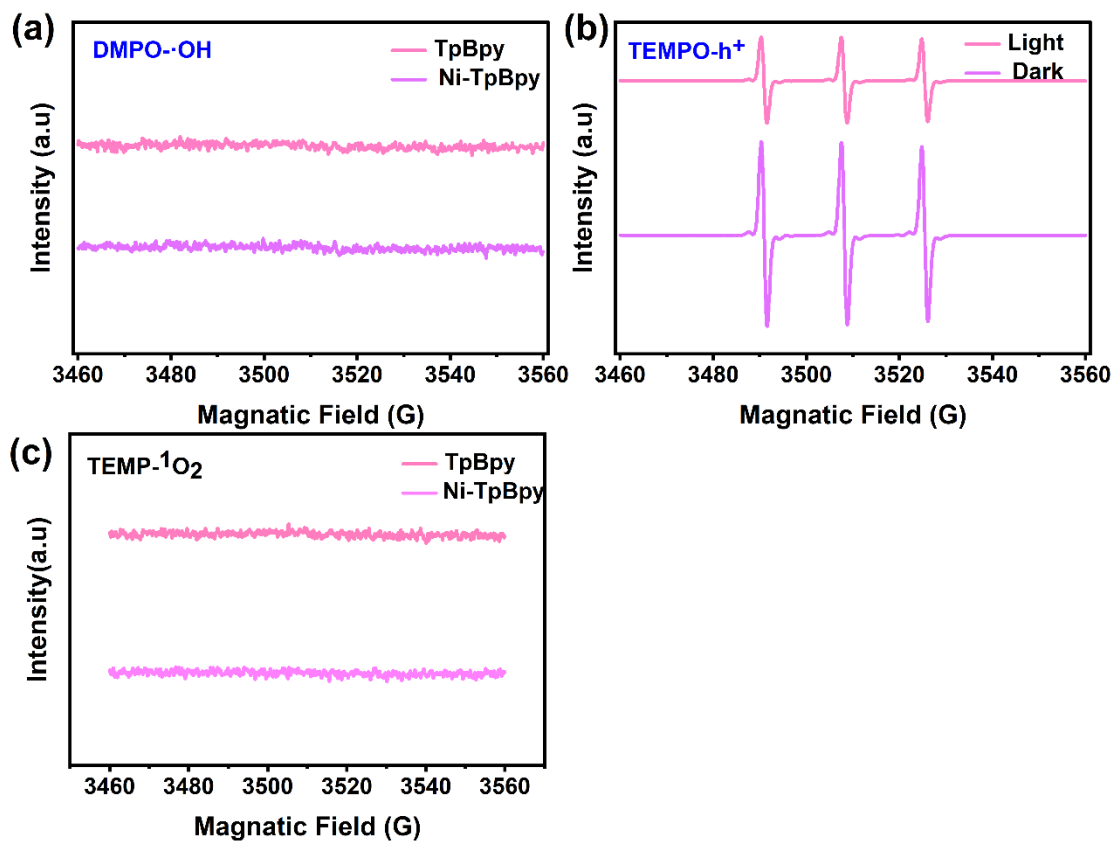


Fig. S18 Effect of anions on the photocatalytic performance of Ni-TpBpy.



**Fig. S19** Photocatalytic performance of Ni-TpBpy for degradation of sulfonamides with concentration of 20 mg/L (a) and the corresponding removal efficiency (b).



**Fig. S20** EPR spectra of ACT degradation on TpBpy and Ni-TpBpy: signals of DMPO- $\cdot$ OH (a), TEMPO- $h^+$  (b) and TEMP- $^1O_2$  (c).



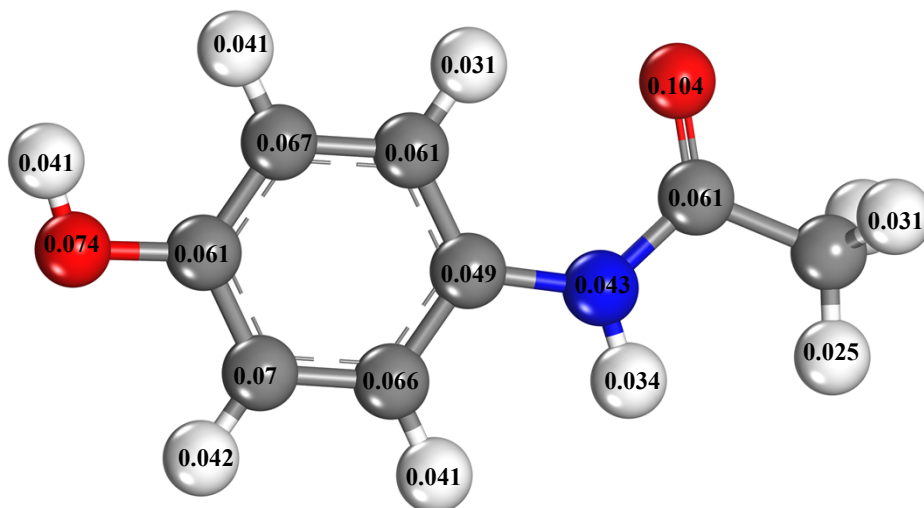


**Fig. S21** Fukui index of ACT.

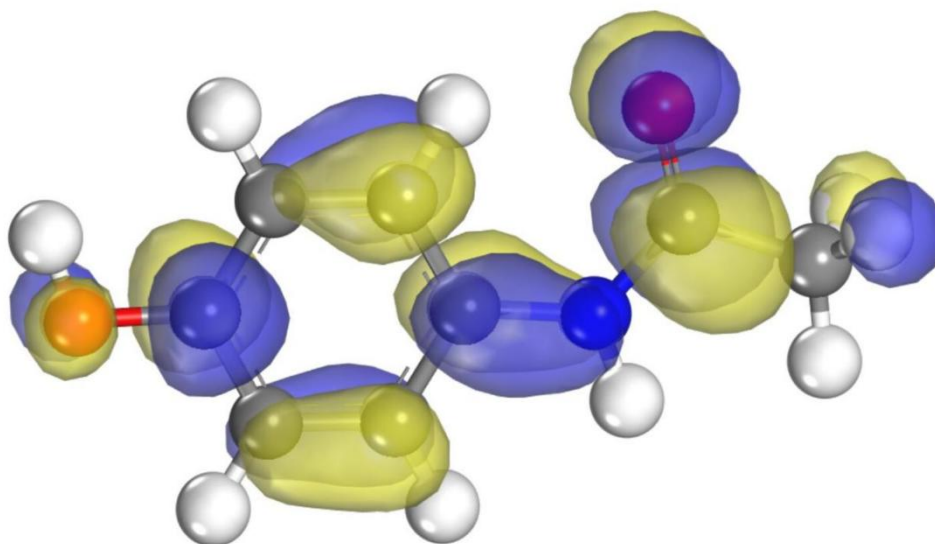


**Fig. S22** LUMO orbitals of ACT.

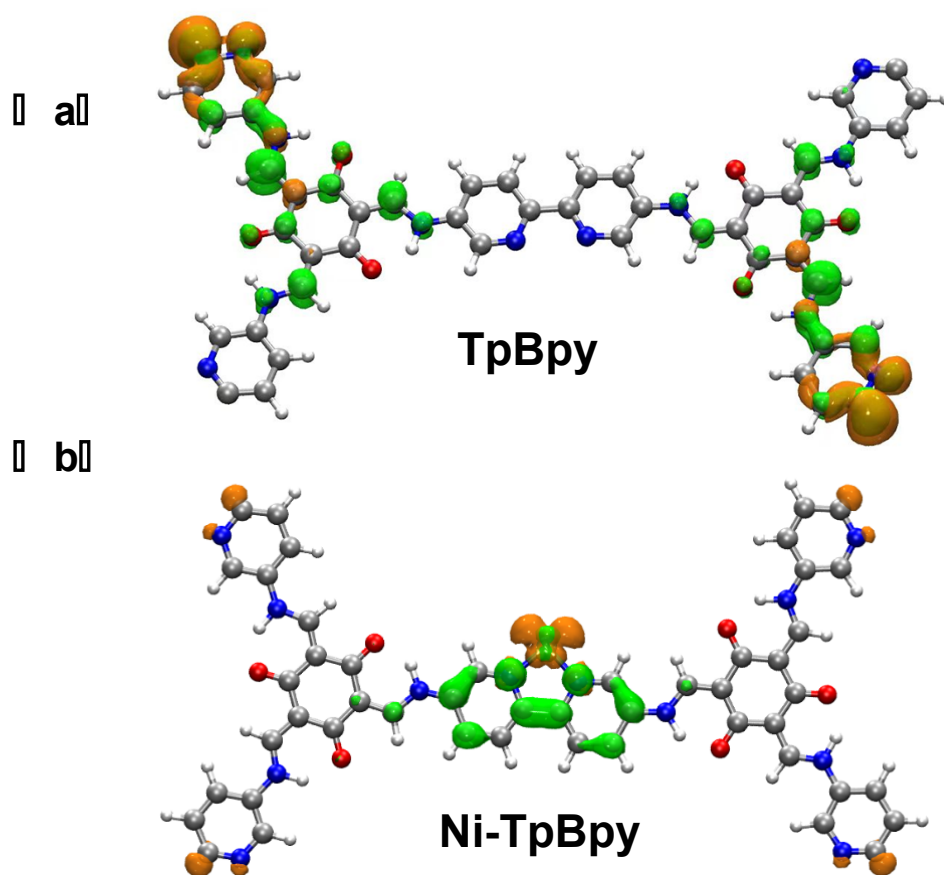


**Fig. 23.** Electron and hole density mapping of TpBpy (a) and Ni-TpBpy (b) in excited state by DFT simulation; note: brown and green isosurfaces represent hole and electron distributions, respectively.

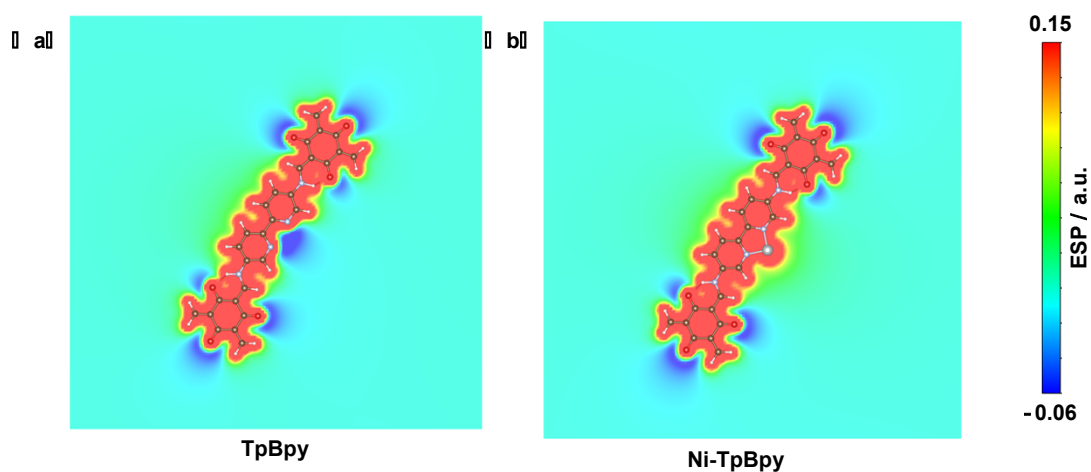


**Fig. S24** Two-dimensional electrostatic potential maps of TpBpy (a) and Ni-TpBpy (b).

## 6. Tables

### 6.1 Structural EXAFS data fitting results of Samples

**Table S1** Structural EXAFS data fitting results of samples.

Sample	Path	CN <sup>a</sup>	R(Å) <sup>b</sup>	σ <sup>2</sup> (Å <sup>2</sup> ) <sup>c</sup>	ΔE <sub>0</sub> (eV) <sup>d</sup>	R factor
Ni K-edge ( $S_0^2=0.777$ )						
Ni foil	Ni-Ni	12*	2.481±0.002	0.0062	7.0	0.0010
NiO	Ni-O	6.0±0.2	2.087±0.014	0.0053	-1.3	0.0055
	Ni-O-Ni	12.1±0.3	2.946±0.006	0.0060	-3.9	
sample-2-Ni	Ni-N	2.3±0.5	2.003±0.019	0.0101	-5.3	0.0065
	Ni-Cl	1.8±0.3	2.188±0.029		-1.3	

<sup>a</sup>CN, coordination number; <sup>b</sup>R, the distance between absorber and backscatter atoms; <sup>c</sup>σ<sup>2</sup>, the Debye Waller factor value; <sup>d</sup>ΔE<sub>0</sub>, inner potential correction to account for the difference in the inner potential between the sample and the reference compound; R factor indicates the goodness of the fit.  $S_0^2$  was fixed to 0.777, according to the experimental EXAFS fit of Ni foil by fixing CN as the known crystallographic value. \* This value was fixed during EXAFS fitting, based on the known structure of Ni. Fitting conditions:  $k$  range : 3.0 - 11.0;  $R$  range: 1.0-2.5; fitting space: R space;  $k$ -weight = 3. A reasonable range of EXAFS fitting parameters:  $0.800 < S_0^2 < 1.000$ ;  $CN > 0$ ;  $\sigma^2 > 0 \text{ \AA}^2$ ;  $|\Delta E_0| < 10 \text{ eV}$ ;  $R \text{ factor} < 0.02$ .

For Wavelet Transform analysis, the  $\chi(k)$  exported from Athena was imported into the Hama Fortran code. The parameters were listed as follow:  $R$ -range, 0.0 - 4.0 Å,  $k$ -range, 0 - 15.0 Å<sup>-1</sup> for sample and Standards;  $k$  weight, 2; and Morlet function with  $\kappa=10$ ,  $\sigma=1$  was used as the mother wavelet to provide the overall distribution.<sup>4</sup> The XAFS data were processed according to the standard procedures using the Athena module implemented in the IFEFFIT software packages. The EXAFS spectra were obtained by subtracting the post-edge background from the overall absorption and then normalizing with respect to the edge-jump step. Subsequently, the  $\chi(k)$  data of were Fourier transformed to real (R) space using a sine windows ( $dk = 1.0 \text{ \AA}^{-1}$ ) to separate the EXAFS contributions from different coordination shells. To obtain the quantitative structural parameters around central atoms, least-squares curve parameter

fitting was performed using the ARTEMIS module of IFEFFIT software packages.<sup>5, 6</sup>

## 6.2 Photoluminescent lifetime determination

**Table S2** Data for photoluminescent lifetime measurement.

Photocatalysts	$\tau_1$ (ns)	$\tau_2$ (ns)	$\tau_3$ (ns)	$\alpha_1$	$\alpha_2$	$\alpha_3$	$\tau_{\text{avg}}$ (ns)
Ni-TpBpy	0.27	1.18	5.68	0.82	0.17	0.0069	0.46
TpBpy	1.16	0.12	6.37	0.14	0.85	0.010	0.32

The time-resolved photoluminescence (TRPL) decay curves for Ni-TpBpy and TpBpy nanomaterials were measured with an emission wavelength of 580 nm, and an excitation wavelength of 406 nm. The average fluorescence lifetime was obtained from  $\tau_{\text{ave}} = \sum \alpha_i \tau_i$ , where  $\tau$  is the fluorescence lifetime and  $\alpha$  the pre-exponential factor.

### 6.3 Comparison of the photocatalytic performance

**Table S3** Summary of heterogeneous catalysts for ACT removal.

Catalyst (g/L)	Light source	ACT (mg/L)	Efficiency	Rate (min <sup>-1</sup> )	TOC/TOC <sub>0</sub>	Ref.
C-Ti catalysts	Simulated	5.0	98.0%	0.067	—	7
0.25	sunlight		180 min			
TGCN	Simulated	50	80%	0.027	100%	8
0.6	sunlight		120 min		120 min	
Bi <sub>2</sub> O <sub>3</sub> /MnO <sub>2</sub>	Visible	5	94.3%	0.020	82.2%	9
1.0	light		120 min		120 min	
ZnFe-CLDH/RGO	Simulated	5	95%	0.007	49.8%	10
0.5	sunlight		420 min		420 min	
TiZr MOF	Simulated	5	99.0%	0.012	65.3%	11
0.25	sunlight		360 min		180 min	
Fe/Co-MOF	Visible	20	97.4%	0.031	—	12
0.5	light		180 min		180 min	
UiO-66-NH-C <sub>5</sub>	Simulated	5	98.0%	0.09	50%	13
0.25	sunlight		240 min		180 min	
r@TiO <sub>2</sub> /UiO-66-NH <sub>2</sub>	Visible	5	93.5%	0.01	55%	14
0.25	light		240 min		600 min	
COF-PDZ	Visible	—	99.8%	0.029	—	15
-	light		180 min		180 min	
COF-TD1	Visible	5	98.3%	0.045	—	16
0.3	light		60 min		60 min	
<b>Ni-TpBpy</b>	<b>Visible</b>	<b>20</b>	<b>97.8%</b>	<b>0.177</b>	<b>56.8%</b>	<b>This</b>
<b>0.3</b>	<b>light</b>		<b>30 min</b>		<b>30 min</b>	

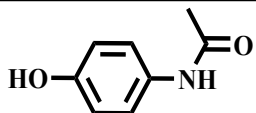
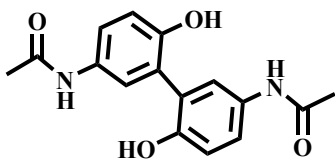
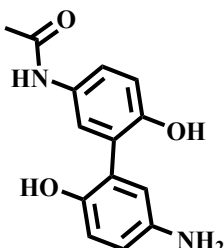
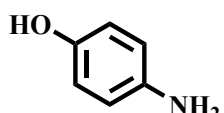
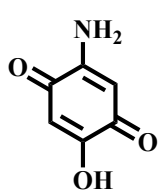
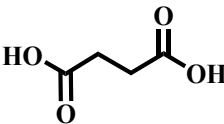
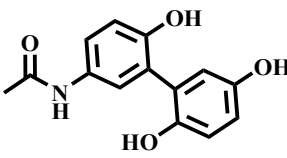
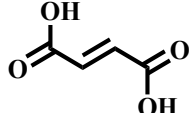
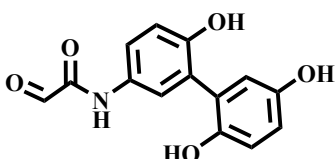
## 6.4 Actual amount of Ni anchored on the TpBpy

**Table S4** Actual amount of Ni anchored on the TpBpy.

<b>Sample</b>	<b>Ni weight amount (wt%)</b>
Ni-TpBpy-1	3.7%
Ni-TpBpy-2	4.6%
Ni-TpBpy-3	5.6%

## 6.5 Intermediates products

**Table S5** List of intermediates products generated in the photodegradation process.

Compound	Elemental composition	Proposed Structure	m/z
ACT	C <sub>8</sub> H <sub>9</sub> NO <sub>2</sub>		151.06
A1	C <sub>16</sub> H <sub>16</sub> N <sub>2</sub> O <sub>4</sub>		300.11
A2	C <sub>14</sub> H <sub>14</sub> N <sub>2</sub> O <sub>3</sub>		258.09
A3	C <sub>6</sub> H <sub>7</sub> NO		109.05
A4	C <sub>6</sub> H <sub>5</sub> NO <sub>3</sub>		125.05
A5	C <sub>4</sub> H <sub>6</sub> O <sub>4</sub>		118.03
A6	C <sub>14</sub> H <sub>13</sub> NO <sub>4</sub>		259.08
A7	C <sub>4</sub> H <sub>4</sub> O <sub>4</sub>		116.01
A8	C <sub>14</sub> H <sub>11</sub> NO <sub>5</sub>		273.06



## 7. Reference

1. J. P. Perdew, K. Burke and M. Ernzerhof, *Phys. Rev. Lett.*, 1996, **77**, 3865-3868.
2. B. Delley, *J. Chem. Phys.*, 2000, **113**, 7756-7764.
3. C. Zhao, Z. Liao, W. Liu, F. Liu, J. Ye, J. Liang and Y. Li, *J. Hazard. Mater.*, 2020, **381**, 120957-120965.
4. H. Funke, M. Chukalina and A. Rossberg, *Phys. Scr.*, 2005, 232-235.
5. B. Ravel and M. Newville, *J. Synchrotron Radiat.*, 2005, **12**, 537-541.
6. S. I. Zabinsky, J. J. Rehr, A. Ankudinov, R. C. Albers and M. J. Eller, *Phys. Rev. B*, 1995, **52**, 2995-3009.
7. A. Gómez-Avilés, M. Peñas-Garzón, J. Bedia, J. J. Rodríguez and C. Belver, *Chem. Eng. J.*, 2019, **358**, 1574-1582.
8. S. Moradi, A. A. Isari, F. Hayati, R. Rezaei Kalantary and B. Kakavandi, *Chem. Eng. J.*, 2021, **414**, 128618-128629.
9. V. K. Parida, S. K. Srivastava, S. Chowdhury and A. K. Gupta, *Chem. Eng. J.*, 2023, **472**, 144969-144989.
10. J. Zhu, Z. Zhu, H. Zhang, H. Lu, W. Zhang, Y. Qiu, L. Zhu and S. Küppers, *Appl. Catal. B: Environ.*, 2018, **225**, 550-562.
11. A. Gómez-Avilés, M. Peñas-Garzón, J. Bedia, D. D. Dionysiou, J. J. Rodríguez and C. Belver, *Appl. Catal. B: Environ.*, 2019, **253**, 253-262.
12. D. Pattappan, A. Mohankumar, R. T. R. Kumar, S. Palanisamy, Y.-T. Lai, Y. S. Huh, J.-J. Shim and Y. Haldorai, *Chem. Eng. J.*, 2023, **464**, 142676-142690.
13. A. Gómez-Avilés, R. R. Solís, E. M. García-Frutos, J. Bedia and C. Belver, *Chem. Eng. J.*, 2023, **461**, 141889-141901.
14. Y. L. Wang, M. Peñas-Garzón, J. J. Rodríguez, J. Bedia and C. Belver, *Chem. Eng. J.*, 2022, **446**, 137229-137240.
15. B. Zhang, F. Liu, C. Nie, Y. Hou and M. Tong, *J. Hazard. Mater.*, 2022, **435**, 128966-128976.
16. Y. Hou, F. Liu, B. Zhang and M. Tong, *Environ. Sci. Technol.*, 2022, **56**, 16303-16314.